analytical chemistry

pubs.acs.org/ac Article

Supramolecular Anchored Copper Nanoclusters for a Multipath Electrochemiluminescence Probe

Xiaoyue Zhang, Xuan Kuang, Xiang Ren, Yuewei Wang, Xuejing Liu,* Yueyun Li,* Huangxian Ju, and Qin Wei*

Cite This: *Anal. Chem.* 2023, 95, 16761−16770 Read Online

ACCESS | Metrics & More | Article Recommendations | Supporting Information

ABSTRACT: Copper nanoclusters (Cu NCs) are highly promising nanomaterials in the field of electrochemiluminescence (ECL). Nevertheless, their limited stability and efficiency have impeded their practical applications. Here, we introduced a novel supramolecular anchoring strategy resulting in the creation of exceptionally stable Cu NCs (CET-Cu NCs) with remarkable ECL properties. Specifically, CET-Cu NCs exhibited a relative ECL efficiency (Φ_{ECL}) of 62% based on the annihilation ECL efficiency of $[Ru(bpy)_3]^{2+}$ (100%), with tripropylamine employed as a coreactant. Moreover, CET-Cu NCs can generate ECL emission through multiple different paths, which enables them to serve as signal probes in a wider range of testing scenarios, thereby enhancing the reliability and robustness of sensing and analytical systems. To demonstrate the practical utility, CET-Cu NCs were selected as an ECL signal probe for a sensing platform that facilitated ultrasensitive detection of progesterone via oriented immobilization technology and antibody/aptamer sandwich assays. This study surmounted the barriers to the practical application of Cu NCs through the implementation of a supramolecular anchoring strategy, thereby providing enhanced utility of Cu NCs in ECL sensing and analysis.

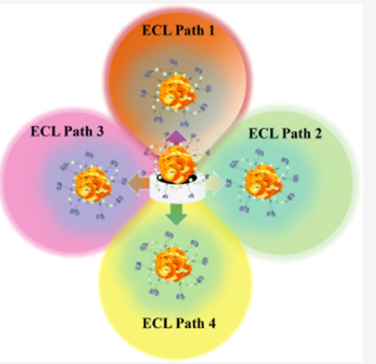

INTRODUCTION

Metal nanoclusters (M NCs) offer significant advantages, including small size,[1,2] low toxicity,[3,4] and unique optical[5,6] and electrical properties,[7] making them increasingly popular in the electrochemiluminescence (ECL) field.[8−10] Copper (Cu), which is abundant in the earth's crust, is an emerging raw material for preparing nanoclusters. However, due to the high reactivity and low standard reduction potential of Cu, achieving stable Cu NCs is an exceptionally difficult task.[11,12] Applying ligands to coat Cu NCs is a reliable approach to enhance their stability,[13] but most ligands protecting Cu NCs are limited to biomolecules, such as DNA[14,15] and proteins[16,17] for this purpose. Utilizing small-molecule ligands to stabilize Cu NCs can effectively diminish the thickness of the insulating layer present on their surface, thereby enhancing the efficiency of carrier transport and, ultimately, augmenting their ECL performance.[18,19] Regrettably, Cu NCs protected by small-molecule ligands generally suffer from inadequate solution stability and a propensity to undergo aggregation and stacking phenomena. To obtain stable, well-dispersed, and high ECL efficiency Cu NCs still remains a challenge in the field of ECL.[20−22] 4,4′-Thiobisbenzenethiol, a small molecule with two thiol groups, is expected to show satisfactory results in protecting Cu NCs by significantly reducing the formation of unsaturated bonds. Ethylenediamine possesses an impressive reducing capability and water solubility. Employing ethylenediamine as a ligand for Cu NCs holds promise in potentially mitigating the negative influences of oxidation and aggregation on the stability of the Cu NCs. Cucurbit[7]uril is a fourth-generation macrocyclic host molecule with unique hydrophobic cavities and highly stable rigid outer shells, as well as molecular recognition and self-assembly properties.[23,24] Using host−guest identification of cucurbit[7]uril to anchor novel supramolecular structures on the surface of Cu NCs could introduce a rigid barrier on the nanocluster surface and reduce nonradiative relaxation of the ligands.[25] In addition, the introduced supermolecular structures can be used as "molecular vessels" to attract hydrophobic coreactant, such as tripropylamine (TPA) or triethylamine, thereby shortening the electron transfer distance between the coreactants and the luminescence center, thus improving the ECL performance of the Cu NCs.

Developing Cu NCs with multipath ECL properties as signal probes for sensing platforms can significantly enhance the reliability and robustness of sensing analysis systems. Should one ECL path fail or become ineffective, other paths can still provide a valid ECL signal, thereby ensuring the accuracy and timeliness of the results. Moreover, the establishment of a multipath ECL probe enables the selection of different ECL

Received: September 12, 2023
Revised: October 11, 2023
Accepted: October 16, 2023
Published: October 31, 2023

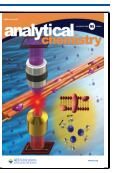

https://doi.org/10.1021/acs.analchem.3c04086
Anal. Chem. 2023, 95, 16761−16770

Scheme 1. Schematic Diagram of the Construction Process of CET-Cu NCs

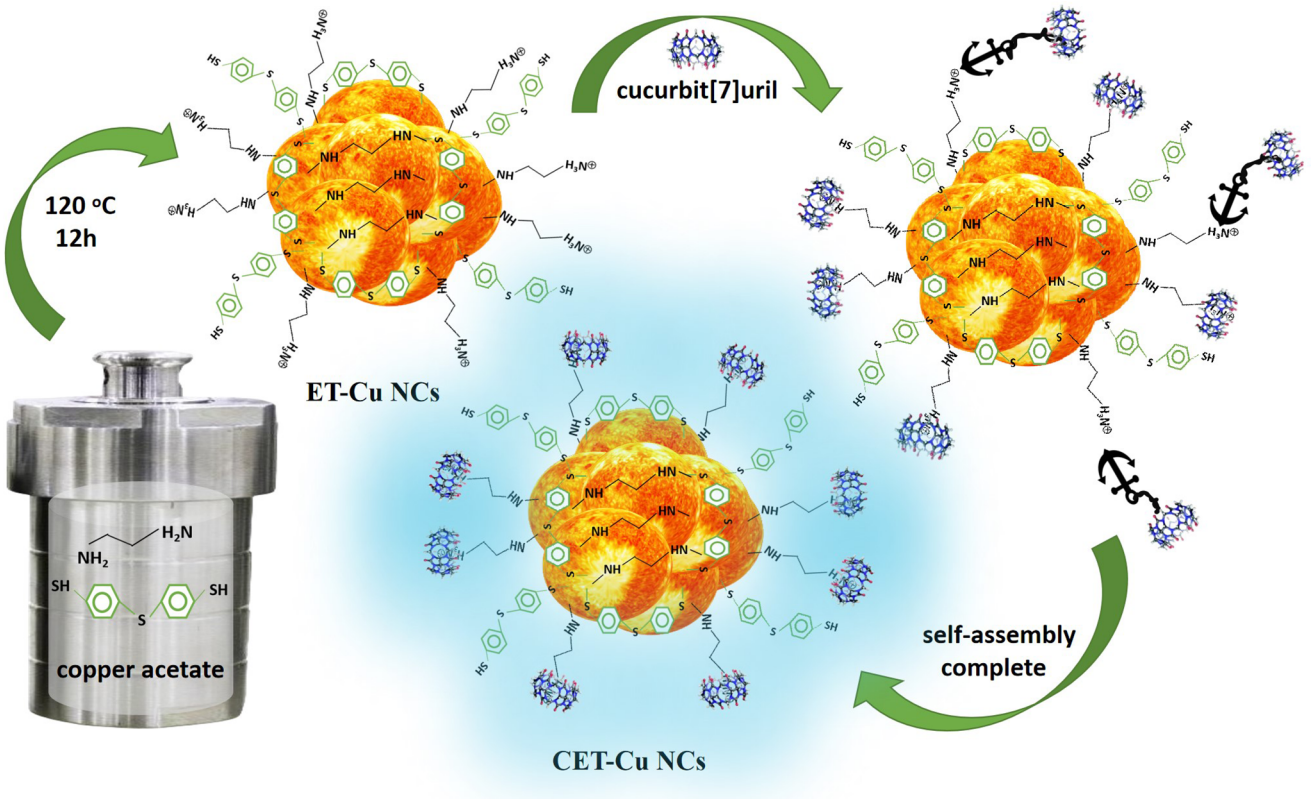

paths according to specific application requirements, which further expands the potential applications.

Environmental steroid hormone contamination has emerged as a pressing challenge to public health.[26,27] Progesterone, a steroid hormone distributed in nature, has significant effects on human well-being. Therefore, it is imperative to develop a sensitive and specific detection method.[28] The antibody/aptamer sandwich method utilizes the advantages of both antibody and aptamer and has a high specificity.[29,30] By combining the aptamer/antibody sandwich method with ECL and the oriented immobilization technology of antibodies, a specific and sensitive determination of progesterone can be achieved.

After thorough consideration of the aforementioned factors, the small-molecule ligands 4,4′-thiobisbenzenethiol and ethylenediamine were utilized as ligands to protect the Cu NCs, and cucurbit[7]uril was used to selectively recognize ethylenediamine, resulting in the anchoring of the supramolecular structure onto the surface of Cu NCs. As a result, novel Cu NCs (CET-Cu NCs, C represents cucurbit[7]uril, E represents ethylenediamine, and T represents 4,4′-thiobisbenzenethiol) were successfully synthesized. This novel supramolecular anchoring strategy not only passivated the surface of the CET-Cu NCs thereby minimizing their surface energy but also effectively suppressed nonradiative relaxation processes that interfere with ECL emission. Moreover, by anchoring the supramolecular structure onto the nanocluster surface, the hydrophobic cavity of the macrocycle facilitates the accumulation of hydrophobic coreactants. This significantly reduces the electron transfer distance between the coreactant and the electrochemiluminophore. The CET-Cu NCs constructed through this supramolecular anchoring strategy exhibited superior luminescence and storage stability and demonstrated multipath ECL emission capabilities. Utilizing the anodic ECL of the CET-Cu NCs, in conjunction with boric acid group-oriented immobilization technology, an innovative method for the sensitive detection of progesterone was successfully developed. The methodology proposed in this study provides a broad prospect for ECL-based sensing and detection.

EXPERIMENTAL SECTION

Reagents and Materials. The reagents used in this study were purchased from a variety of sources. Copper acetate was obtained from Tianjin Kermel Chemical Reagent Co., Ltd., while ethylenediamine, *N*,*N*-dimethylformamide, disodium hydrogen phosphate, acetonitrile, potassium dihydrogen phosphate, and ethanol were purchased from Sinopharm Chemical Reagent Co., Ltd. Bovine serum albumin (BSA) was obtained from Shanghai Aladdin Bio-Chem Technology Co., Ltd. 4,4′-Thiobisbenzenethiol, cucurbit[7]uril, tripropylamine (TPA), potassium persulfate ($K_2S_2O_8$), progesterone, 3-aminobenzeneboronic acid (3-ABA), estradiol (E2), bisphenol A (BPA), and tetrabutylammonium hexafluorophosphate (TBAPF6) were purchased from Shanghai Macklin Biochemical Technology Co., Ltd. Microcystin-LR (MC) was purchased from Shanghai Acmec Biochemical Co., Ltd.. Sodium fluoride (NaF) was obtained from Tianjin Damao Chemical Reagent Co., Ltd. Progesterone antibody (Ab) was purchased from Nanjing Okay Biotechnology Co., Ltd. The progesterone-binding DNA aptamer (aptamer) was purchased from Sangon Biotech (Shanghai) Co., Ltd. The sequence of aptamer was as follows (from 5′ to 3′): GATTAACAT-TAGCCCACCGCCCACC-NH_2.[31]

Apparatus. The morphology and internal structures of Cu NCs were characterized by a high-resolution transmission electron microscope (HRTEM, JEOL). The absorption

https://doi.org/10.1021/acs.analchem.3c04086
Anal. Chem. 2023, 95, 16761−16770

Scheme 2. Schematic Diagram of the Sensing Platform

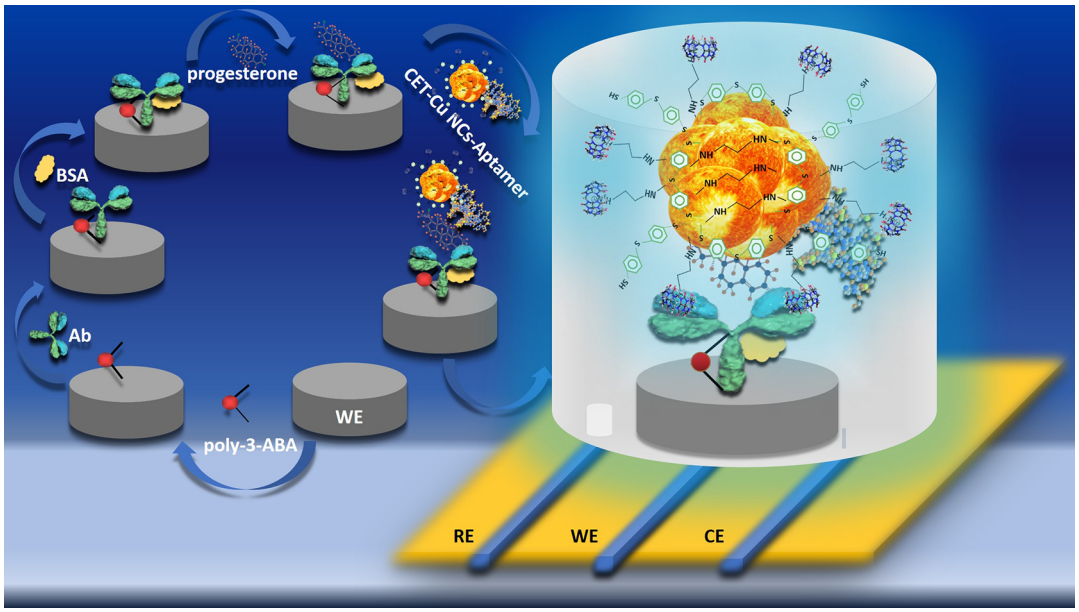

properties of infrared radiation of Cu NCs were measured by an FT-IR-410 infrared spectrometer (JASCO). The optical properties of Cu NCs were characterized by UV−vis spectrometry (PerkinElmer) and LS-45/55 PL spectrometer (PerkinElmer). The proton nuclear magnetic resonance spectra (H-NMR) of Cu NCs were obtained by a Bruker AVANCE III 400 M NMR spectrometer. The relevant ECL measurements were performed in the ECL analyzer (Xi'an Remax Analysis Instruments Co., Ltd.). The electrochemical tests were performed using an electrochemical workstation (Zahner Zennium PP211).

Preparation of CET-Cu NCs. To prepare the CET-Cu NCs, the following steps were performed: 10 mL of *N*,*N*-dimethylformamide containing 0.6 mM 4,4′-thiobisbenzenethiol, which had been prepared in advance, was added to 10 mL of an aqueous solution of 0.3 mM copper acetate. Subsequently, 10 mL of a 2.4 mM aqueous solution of ethylenediamine was slowly added to the mixture, and stirring was continued until the mixture became homogeneous. The homogeneous mixture was then transferred to a reaction vessel and heated at 120 °C for 12 h. After the reaction, 10 mL of the product was then taken and filtered. The filtrate was then dialyzed. Next, 10 mL of the dialyzed product was added to 2 mL of 2.4 mM cucurbit[7]uril in water. The resulting mixture was stirred for 2 h. To purify the CET-Cu NCs, dialysis was performed (Scheme 1).

Preparation of CET-Cu NC-Aptamer. 500 μL of CET-Cu NCs mixed with 500 μL of 10 μM aptamer was shaken at 37 °C for 12 h.

Fabrication of the Progesterone Sensing Platform. The sensing platform used pH 7.4 PBS containing 10 mM TPA as the testing buffer. A three-electrode system was used with Ag/AgCl as the reference electrode (RE), a Pt electrode as the counter electrode (CE), and the modified glassy carbon electrode (GCE) as the working electrode (WE). The WE was placed in PBS containing 50 mM of 3-ABA and 150 mM NaF, and electrochemical polymerization was carried out at a potential of −0.2−0.7 V. After washing, the electrode was modified with 8 μL of 10 μg/mL Ab solution and left to stand for 50 min, followed by washing. Then, 6 μL of 0.1% BSA was added, and the electrode surface was cleaned after 30 min. Different concentrations of progesterone were added to the modified electrode surface. After incubation for 50 min, the electrode was washed. Finally, 8 μL of CET-Cu NC-aptamer was added and incubated for 50 min, and the modified WE preparation was completed after washing (Scheme 2).

Parameter setting of the sensing platform: The voltage of the photomultiplier tube was set to 600 V, and the scan rate was set to 0.5 V/s.

Sample Handling Procedure. Tap water collected from the water supply network was filtered through a 0.45 μm microporous membrane and used as a sample for testing.

RESULTS AND DISCUSSION

Characterization of the Anchoring Process. The interaction between cucurbit[7]uril and Cu NCs was studied by comparing the H-NMR. As shown in the H-NMR of unanchored Cu NCs (ET-Cu NCs, E represents ethylenediamine, T represents 4,4′-thiobisbenzenethiol) (Figure S1), initial resonances (7.831−8.348 ppm) corresponded to hydrogen in benzene rings, amino groups, and thiol groups. Chemical shifts around 3.232 and 2.667−3.217 ppm correspond to the hydrogen on methylene and methyl groups. The H-NMR of CET-Cu NCs shows changes in intensity and chemical shift, suggesting structural changes and adjustments in the coordination environment due to cucurbit[7]uril anchoring. A novel resonance signal at 3.324 ppm, generated by unique methine in cucurbit[7]uril, provided evidence for successful anchoring (Figure S2). The infrared spectrum showed a partial suppression of vibration of ligands' functional groups on the surface of ET-Cu NCs after cucurbit[7]uril fixation (Figure S3). Specifically, when cucurbit[7]uril was anchored on the surface of the ET-Cu NCs, the characteristic peak intensity of N−H stretching vibration (3750−3000 cm^{-1}) and C−N stretching vibrations (1340 cm^{-1}) became weaker, indicating that the binding site of supramolecular structure may be located on the ethylenediamine. Furthermore, the out-of-plane bending vibration of the C−H bond of the benzene

https://doi.org/10.1021/acs.analchem.3c04086
Anal. Chem. 2023, 95, 16761−16770

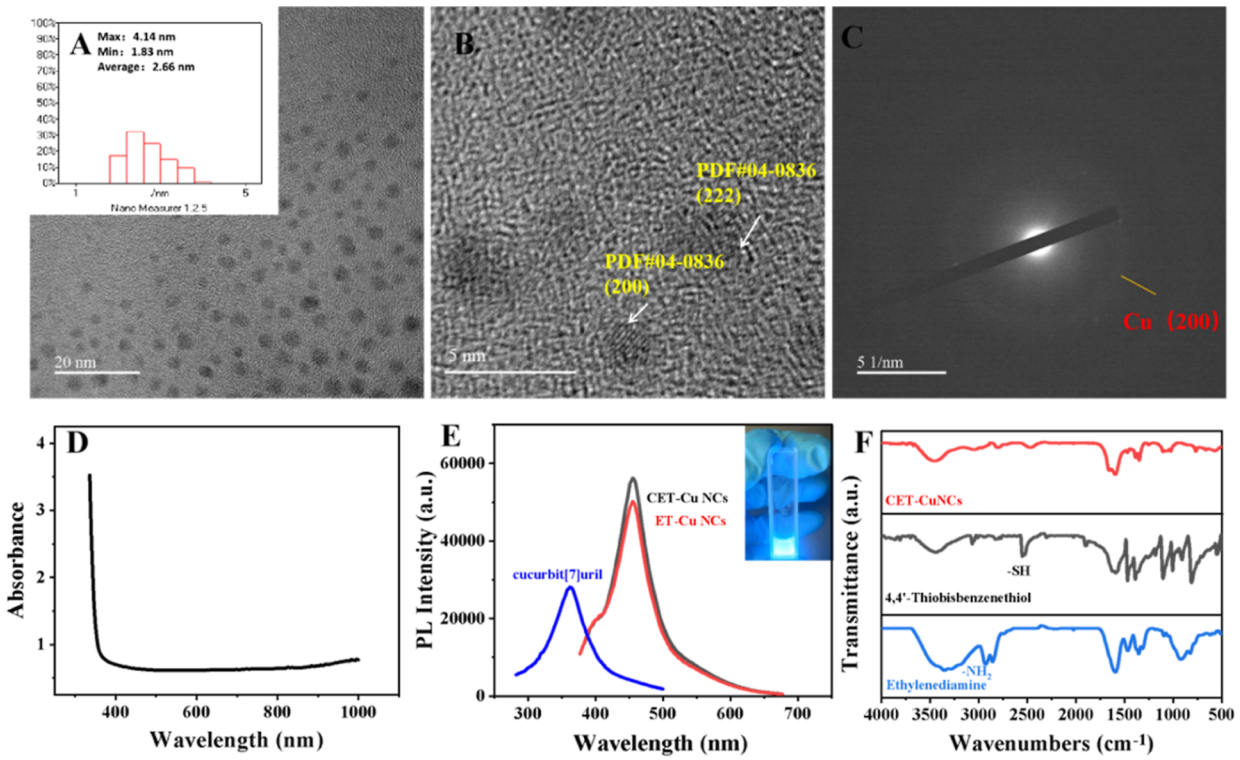

Figure 1. TEM of CET-Cu NCs (A), HRTEM of CET-Cu NCs (B), selected area electron diffraction (SAED) of CET-Cu NCs (C), UV−vis absorption of CET-Cu NCs (D), and PL spectra of CET-Cu NCs (black curve), ET-Cu NCs (red curve), and cucurbit[7]uril (blue curve) (E). Infrared spectrum of CET-Cu NCs (red curve), 4,4′-thiobisbenzenethiol (black curve), and ethanediamine (blue curve) (F).

ring was suppressed at 771 cm^{-1} after cucurbit[7]uril anchoring, suggesting that the macrocyclic host may also affect the vibration of 4,4′-thiobisbenzenethiol. These findings provide evidence of the successful anchoring of cucurbit[7]uril on the surface of ET-Cu NCs.

Characterization of CET-Cu NCs. The TEM characterization of CET-Cu NCs was conducted, which revealed that the synthesized Cu NCs had a relatively uniform morphology, as shown in Figure 1A. The particle sizes ranged from 1.83 to 4.14 nm, with an average of 2.66 nm. The HRTEM images in Figure 1B demonstrated that the CET-Cu NCs had a good crystal structure with (200) and (222) crystal planes of Cu exposed (PDF#04−0836). Figure 1C displays diffraction data that provide further evidence of the (200) crystal plane of Cu. As the sizes of the CET-Cu NCs were close to the electron Fermi wavelength, the electron motion in the particles was significantly restricted. Consequently, we did not observe a characteristic absorption peak of Cu nanoparticles at 500−600 nm in the UV−vis spectrum (Figure 1D), which indirectly confirmed the successful synthesis of the nanoclusters. Under excitation at a wavelength of 280 nm, cucurbit[7]uril exhibits a fluorescence emission at 362 nm. Interestingly, the maximum fluorescence emission wavelength and peak shape of the ET-Cu NCs remained unchanged after being anchored with cucurbit[7]uril. This indicates that the process of anchoring does not significantly affect the fluorescence properties of the ET-Cu NCs. Excited with a wavelength of 365 nm, the CET-Cu NCs emitted vivid blue fluorescence, with a maximum emission wavelength of 456 nm (Figure 1E). Infrared spectroscopy was utilized to analyze the CET-Cu NCs (Figure 1F). The infrared characteristic absorption peak of the thiol groups of pure 4,4′-thiobisbenzenethiol was observed at 2557 cm^{-1}, and a weak vibration peak of thiol groups was also detected in the CET-Cu NCs. This indicates that not all of the thiol groups were bound to Cu through Cu−S bonds, and some unbound thiol groups remained on the surface of the Cu NCs. The characteristic N−H stretching vibration absorption peak of ethylenediamine appeared in the range of 3750−3000 cm^{-1}, and a faint amino group feature peak was also observed in the infrared spectra of CET-Cu NCs. These experimental results provide information about the ligand groups on the surfaces of CET-Cu NCs. To provide evidence of the stability of the Cu NCs, the storage time of two types of Cu NCs was extended to 4 months. Subsequently, we captured photographs of two types of nanoclusters in the aqueous phase under natural light and fluorescence images of two types of nanoclusters under UV light. Our observations revealed that ET-Cu NCs exhibited flocculent precipitation, accompanied by a decrease in fluorescence intensity. In contrast, CET-Cu NCs showed no noticeable changes over the storage period (Figure S4). Additionally, the morphology information on the nanoclusters was examined using TEM after a storage period of 4 months in an aqueous environment. TEM confirmed that CET-Cu NCs maintained their original particle size and morphology, while ET-Cu NCs displayed aggregation phenomena (Figure S5).

Multipath ECL Properties of CET-Cu NCs. The ECL properties of the CET-Cu NCs were investigated. It was surprising to find that various ECL emission paths were exhibited by the synthesized nanoclusters. Figure 2A illustrates the ligand-triggered ECL emission data of the CET-Cu NCs. Without the participation of coreactants, the CET-Cu NCs could achieve anodic ECL emission. By performing cyclic voltammetry (CV) scanning from 0 to 1.6 V in 0.1 M PBS (Figure 2B), we can observe that the CET-Cu NCs start to release photons at 1.06 V and reach the peak at 1.60 V (Figure

https://doi.org/10.1021/acs.analchem.3c04086
Anal. Chem. 2023, 95, 16761−16770

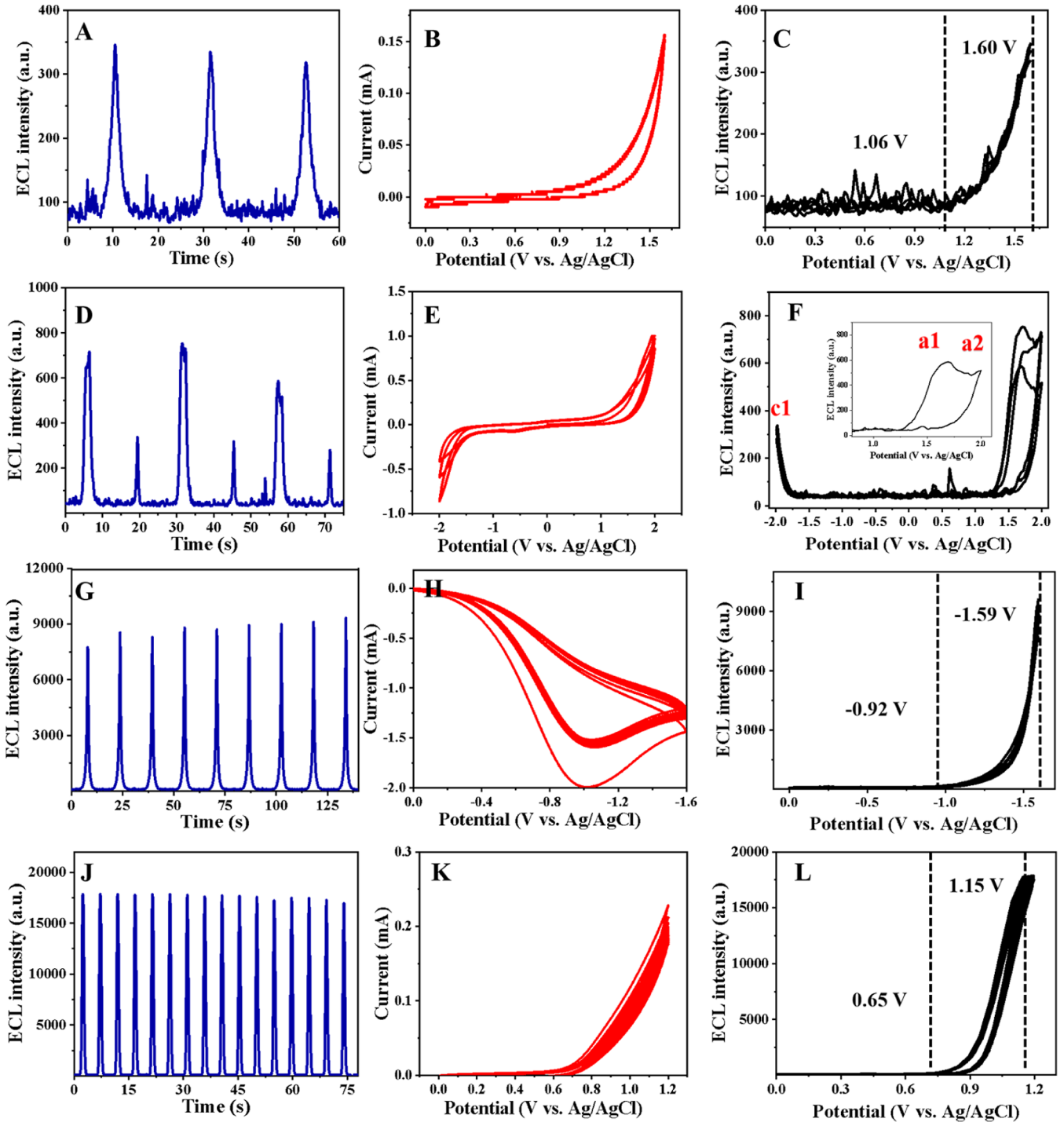

Figure 2. ECL−time curve (A), CV curve (B), and ECL−potential curve (C) of CET-Cu NCs in ligand-triggered ECL path. ECL−time curve (D), CV curve (E), and ECL−potential curve (F) of CET-Cu NCs in annihilation ECL path. ECL−time curve (G), CV curve (H), and ECL−potential curve (I) of CET-Cu NCs in the path of 80 mM $K_2S_2O_8$ as a coreactant. ECL−time curve (J), CV curve (K), and ECL−potential curve (L) of CET-Cu NCs in the path of 10 mM TPA as a coreactant.

2C). In addition, CET-Cu NCs can also release photons by the annihilation path (Figure 2D). Under continuous triangular wave scanning in the range of −2 to 2 V (Figure 2E), CET-Cu NCs acquire electrons to form the reduced state species at −1.45 V (Figure S6), while oxidized state species are clearly formed at 1.31 and 1.92 V, respectively (Figure S7). The oxidized state species and reduced state species annihilation lead to the formation of excited states, which subsequently undergo radiation relaxation upon returning to the ground state. This is depicted in Figure 2F by two anodic ECL emissions, denoted as a1 and a2, and one cathodic ECL emission (c1). It is proved that there were two hole injection processes and one electron injection process in the annihilation ECL of CET-Cu NCs. The synthesized nanoclusters exhibit stable cathodic ECL emission in the presence of 80 mM $K_2S_2O_8$ as the coreactant (Figure 2G). Under the cyclic scan of 0 to −1.6 V (Figure 2H), accompanying the reduction of $K_2S_2O_8$, the cathodic ECL emission starts at −0.92 V and

https://doi.org/10.1021/acs.analchem.3c04086
Anal. Chem. 2023, 95, 16761−16770

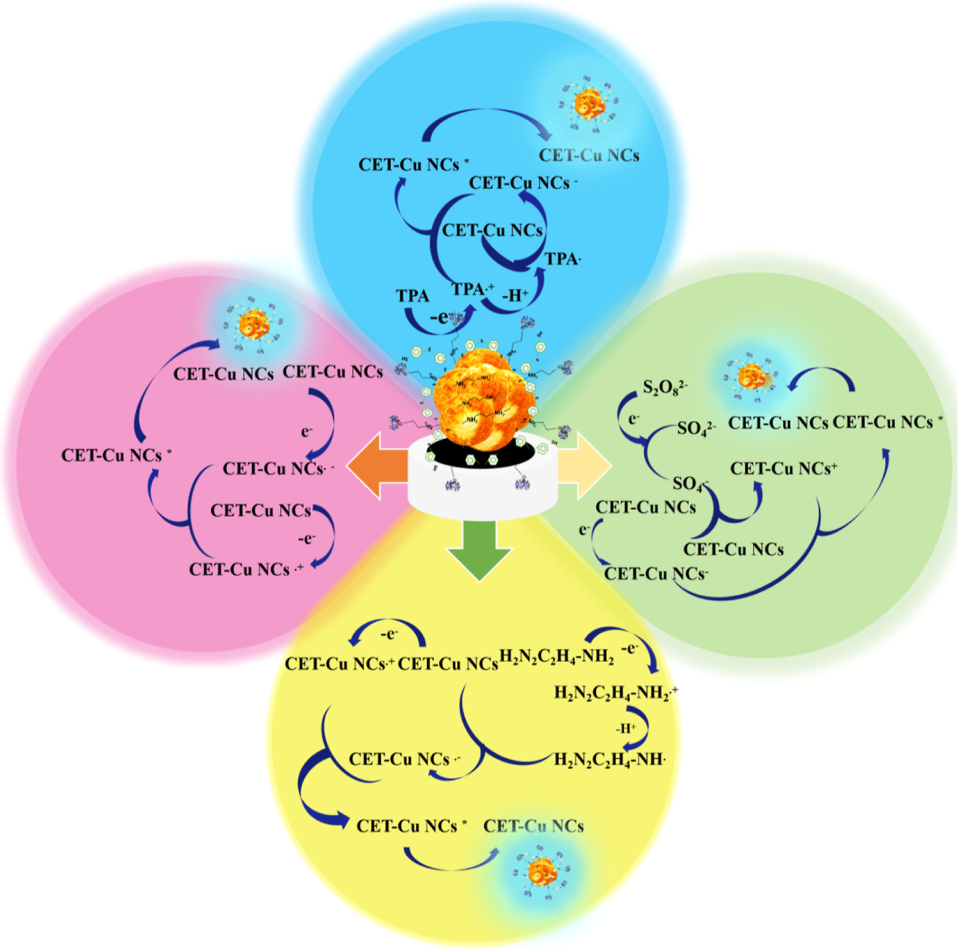

Figure 3. Schematic diagram of the ECL mechanism of CET-Cu NCs.

exhibits intense emission at −1.59 V (Figure 2I). Figure 2J shows the data on the stability of the anodic ECL of CET-Cu NCs under the condition of using 10 mM TPA as the coreactant. After 16 consecutive scans in the potential range of 0−1.2 V (Figure 2K), the ECL signal of the CET-Cu NCs remains stable. The onset potential and peak potential for the anodic ECL of CET-Cu NCs were 0.65 and 1.15 V, respectively (Figure 2L). The excellent anodic ECL performance of CET-Cu NCs in the presence of TPA may be attributed to two factors: first, the surface energy of nanoclusters was reduced due to the anchoring of the supramolecular structure on the surface; second, the supramolecular structure was anchored on the surface of the nanoclusters, which can enrich more TPA, due to the hydrophobic cavity of the macrocycle, thereby shortening the electron transfer distance between the coreactant and the electrochemiluminophore.

The ECL properties of cucurbit[7]uril were thoroughly examined, focusing on ECL emission with TPA as a coreactant, ECL emission induced by annihilation, and anode ECL emission without a coreactant (Figure S8). Surprisingly, the results indicate that cucurbit[7]uril does not exhibit any significant ECL emission through these paths. The ET-Cu NCs demonstrated the ability to generate ECL through multiple paths (Figure S9). However, compared with CET-Cu NCs, the ECL intensity and luminescence stability of ET-Cu NCs are relatively weak. It is worth noting that the luminescence intensity of ET-Cu NCs in the ligand-triggered ECL path is slightly higher than that of CET-Cu NCs. This may be because part of the ethylenediamine ligands on the surface of CET-Cu NCs formed anchored supramolecular structures with cucurbit[7]uril, which affected the number of ligands involved in the ECL luminescence process. In addition, after a 4 month storage in an aqueous solution, we conducted an evaluation of the ECL performance of the nanoclusters under the condition of 10 mM TPA as a coreactant. It is noteworthy that the CET-Cu NCs exhibited consistent ECL signals compared to those of the freshly synthesized CET-Cu NCs, indicating a stable ECL behavior. In contrast, the ECL signal of the ET-Cu NCs showed a significant decline after the 4 month storage period, indicative of a diminished ECL performance over time (Figure S10). These findings emphasize the significant impact of the anchoring process on the ECL properties of ET-Cu NCs, resulting in enhanced ECL intensity and stability.

To further investigate the ECL performance of CET-Cu NCs, the relative ECL efficiency (Φ_{ECL}) of CET-Cu NCs under different ECL paths was tested. The Φ_{ECL} was determined using the formula below

$$\Phi_{ECL} = \Phi^0_{ECL}(Q_f{}^0 I/Q_f I^0)$$

here, $\Phi^0{}_{ECL}$ represented the ECL efficiency of 1 mM $[Ru(bpy)_3]^{2+}$ in 0.1 M $TBAPF_6$/acetonitrile through annihilation, and its value was set as 100%. I and I^0 indicated the

https://doi.org/10.1021/acs.analchem.3c04086
Anal. Chem. 2023, 95, 16761−16770

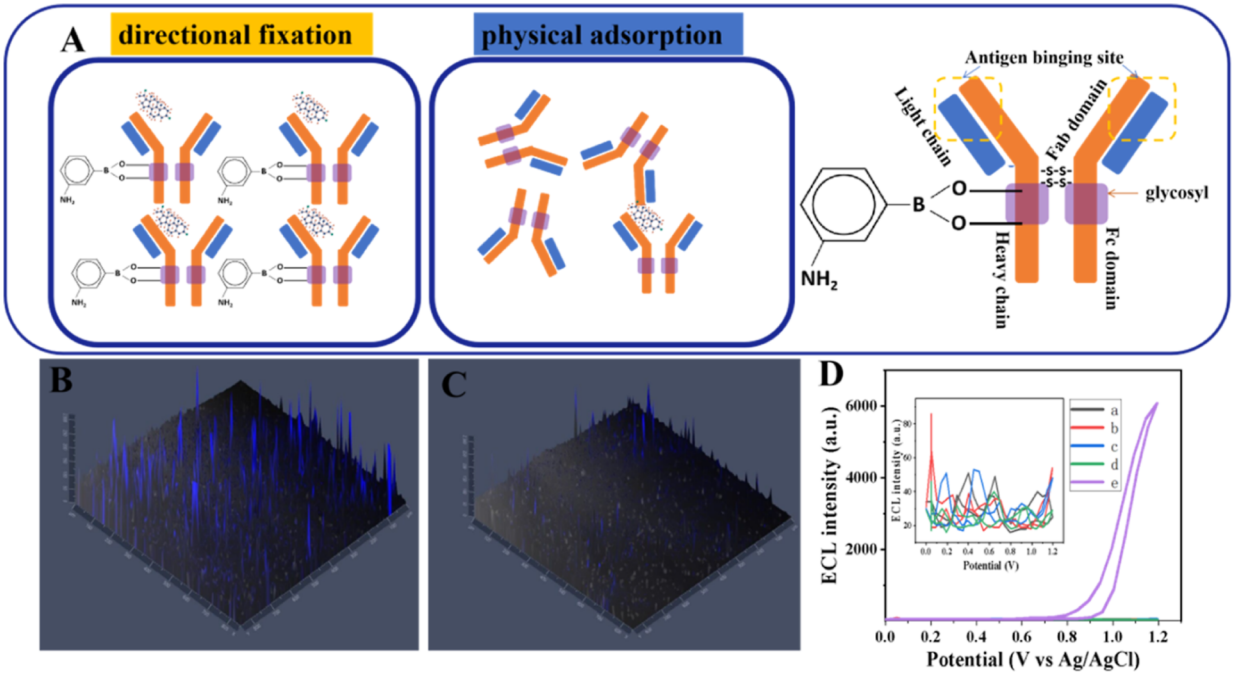

Figure 4. Schematic diagram of the effect of oriented antibody immobilization based on the boric acid group and antibody immobilization based on physical adsorption (A). Simulating the modification process of the sensing platform, laser confocal data obtained by different antibody immobilization techniques: oriented antibody immobilization based on the boric acid group (B). Antibody immobilization based on physical adsorption (C). ECL−potential curve obtained by layer modification of WE (D), poly-3-ABA/GCE (curve a), Ab/poly-3-ABA/GCE (curve b), BSA/Ab/poly-3-ABA/GCE (curve c), progesterone/BSA/Ab/poly-3-ABA/GCE (curve d), and CET-Cu NCs-aptamer/progesterone/BSA/Ab/poly-3-ABA/GCE (curve e).

ECL intensity of the electrochemiluminophore and $[Ru(bpy)_3]^{2+}$, respectively. Q_f and Q_f^0 referred to the corresponding Faraday charges passed by the electrochemiluminophore and $[Ru(bpy)_3]^{2+}$, respectively.

The results indicate that within the potential range of 0−1.6 V, the Φ_{ECL} of CET-Cu NCs in the ligand-triggered ECL path was 3%. The Φ_{ECL} of CET-Cu NCs for annihilation of ECL in the potential range of −2 to 2 V was 2%. When 80 mM $K_2S_2O_8$ was used as a coreactant, the Φ_{ECL} of CET-Cu NCs reached 38%. Remarkably, under the condition of 10 mM TPA as a coreactant, the Φ_{ECL} of nanoclusters could even reach 62%. This high anodic Φ_{ECL} could be attributed to the effective electron transfer between the coreactant and the electrochemiluminophore. The Φ_{ECL} and ECL luminescence stability of ET-Cu NCs were compared when using 10 mM TPA as a coreactant (Figures S11 and S12). The results indicated that the Φ_{ECL} of ET-Cu NCs was only 42%, highlighting that the supramolecular anchoring strategy could improve the Φ_{ECL} and luminescence stabilities of the Cu NCs.

Possible ECL Mechanism of CET-Cu NCs. CET-Cu NCs can generate ECL emission through multiple paths (Figure 3). The ECL mechanism of CET-Cu NCs was explained as follows when TPA was used as a coreactant.[32] Around the electrode, TPA loses an electron to produce $TPA^{\bullet+}$ (eq 1). $TPA^{\bullet+}$ undergoes deprotonation and then transfers electrons to the CET-Cu NCs, causing the CET-Cu NCs to form CET-Cu NCs^- (eqs 2 and 3). CET-Cu NCs^- then reacts with $TPA^{\bullet+}$ generated on the electrode surface to form excited Cu NCs* and emit ECL when they return to the ground state (eqs 4 and 5).

$$TPA \rightarrow TPA^{\bullet+} + e^- \quad (1)$$

$$TPA^{\bullet+} \rightarrow TPA^{\bullet} + H^+ \quad (2)$$

$$CET-Cu\ NCs + TPA^{\bullet} \rightarrow CET-Cu\ NCs^- \quad (3)$$

$$CET-Cu\ NCs^- + TPA^{\bullet+} \rightarrow CET-Cu\ NCs^* \quad (4)$$

$$CET-Cu\ NCs^* \rightarrow CET-Cu\ NCs + h\nu \quad (5)$$

When $K_2S_2O_8$ was employed as a coreactant, the ECL emission path of CET-Cu NCs was presented.[33] $S_2O_8^{2-}$ was reduced to produce an oxidant $SO_4^{\bullet-}$ (eq 6), which then reacts with the CET-Cu NCs to produce CET-Cu NCs^+ (eq 7). At the same time, some CET-Cu NCs gain electrons on the electrode surface, forming CET-Cu NCs^- (eq 8). CET-Cu NCs^- and CET-Cu NCs^+ form an excited state of CET-Cu NCs* (eq 9), accompanied by strong ECL emission when the CET-Cu NCs* return to the ground state (eq 10).

$$S_2O_8^{2-} + e^- \rightarrow SO_4^{2-} + SO_4^{\bullet-} \quad (6)$$

$$CET-Cu\ NCs + SO_4^{\bullet-} \rightarrow CET-Cu\ NCs^+ + SO_4^{2-} \quad (7)$$

$$CET-Cu\ NCs + e^- \rightarrow CET-Cu\ NCs^- \quad (8)$$

$$CET-Cu\ NCs^+ + CET-Cu\ NCs^- \rightarrow CET-Cu\ NCs^* \quad (9)$$

$$CET-Cu\ NCs^* \rightarrow CET-Cu\ NCs + h\nu \quad (10)$$

Without the addition of a coreactant, the synthesized CET-Cu NCs were still capable of achieving anodic ECL emission. We speculated that ethylenediamine ($H_2NC_2H_4-NH_2$) on the surface of CET-Cu NCs was involved in the ECL process of the nanoclusters. Therefore, we refer to it as ligand-triggered ECL. The mechanism of ligand-triggered ECL was explained as

https://doi.org/10.1021/acs.analchem.3c04086
Anal. Chem. 2023, 95, 16761−16770

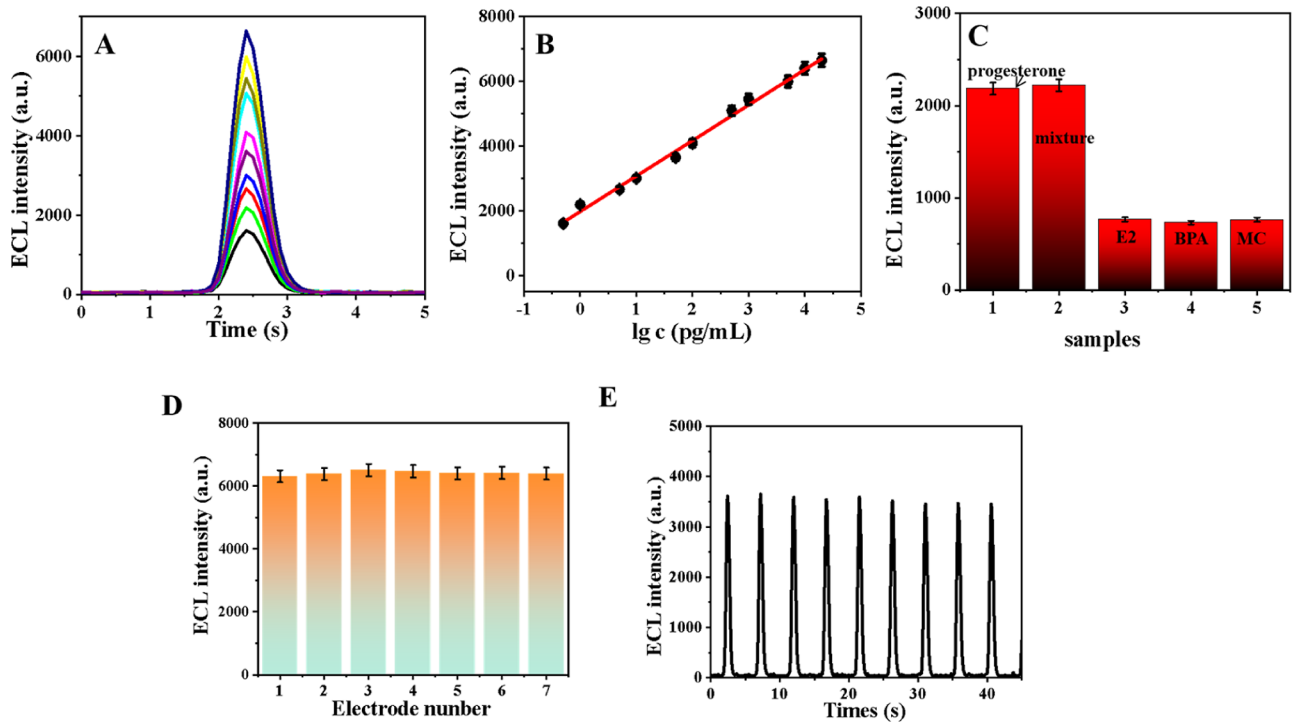

Figure 5. Response value curve of the sensing platform to different concentrations of progesterone (A) and the corresponding working curve (B). Test data were obtained for sensing platform selectivity (C), reproducibility (D), and operational stability (E). Error bars: ± standard deviation, n = 5.

follows:[34] first, $H_2NC_2H_4-NH_2$ was electrochemically oxidized to $H_2NC_2H_4-NH_2^{\bullet+}$ on the electrode surface (eq 11). At the same time, some CET-Cu NCs were oxidized to CET-Cu $NCs^{\bullet+}$ on the electrode surface (eq 12). $H_2NC_2H_4-NH_2^{\bullet+}$ undergoes a deprotonation reaction to generate $H_2NC_2H_4-NH^{\bullet}$ (eq 13), which reacts with some unoxidized CET-Cu NCs to form CET-Cu $NCs^{\bullet-}$ (eq 14). CET-Cu $NCs^{\bullet-}$ encounters CET-Cu $NCs^{\bullet+}$ to produce an excited state of the nanoclusters, which can emit ECL when it returns to the ground state (eqs 15 and 16).

$$H_2NC_2H_4 - NH_2 - e^- \rightarrow H_2NC_2H_4 - NH_2^{\bullet+} \quad (11)$$

$$\text{CET}-\text{Cu NCs} - e^- \rightarrow \text{CET} - \text{Cu NCs}^{\bullet+} \quad (12)$$

$$H_2NC_2H_4 - NH_2^{\bullet+} \rightarrow H_2NC_2H_4 - NH^{\bullet} + H^+ \quad (13)$$

$$\text{CET}-\text{Cu NCs} + H_2NC_2H_4 - NH^{\bullet} \rightarrow \text{CET} - \text{Cu NCs}^{\bullet-} \quad (14)$$

$$\text{CET}-\text{Cu NCs}^{\bullet-} + \text{CET} - \text{Cu NCs}^{\bullet+} \rightarrow \text{CET} - \text{Cu NCs}^{*} \quad (15)$$

$$\text{CET}-\text{Cu NCs}^{*} \rightarrow \text{CET} - \text{Cu NCs} + h\nu \quad (16)$$

The annihilation ECL of CET-Cu NCs was based on the following mechanism:[35] CET-Cu NCs gain an electron to become CET-Cu $NCs^{\bullet-}$ at −1.45 V and lose an electron to become CET-Cu $NCs^{\bullet+}$ at 1.31 and 1.92 V (eqs 17 and 18). The generated free radicals undergo an annihilation reaction to produce an excited state, which emits ECL upon returning to the ground state (eqs 19 and 20).

$$\text{CET}-\text{Cu NCs} + e^- \rightarrow \text{CET} - \text{Cu NCs}^{\bullet-} \quad (17)$$

$$\text{CET}-\text{Cu NCs} - e^- \rightarrow \text{CET} - \text{Cu NCs}^{\bullet+} \quad (18)$$

$$\text{CET}-\text{Cu NCs}^{\bullet-} + \text{CET} - \text{Cu NCs}^{\bullet+} \rightarrow \text{CET} - \text{Cu NCs}^{*} \quad (19)$$

$$\text{CET}-\text{Cu NCs}^{*} \rightarrow \text{CET} - \text{Cu NCs} + h\nu \quad (20)$$

Feasibility Characterization of the Sensing Platform. A platform was developed to detect progesterone using CET-Cu NCs as anode ECL probes with TPA as a coreactant. The efficient immobilization of antibodies played a critical role in the recognition of the target,[36] which in turn determines the performance of the sensing platform. The Fc fragment of antibodies contained glycan chains that can form stable pentagonal ring structures with boronic acid groups under weak alkaline conditions (Figure 4A). To this end, we employ electropolymerized 3-ABA (poly-3-ABA) on the electrode surface to accomplish simple oriented immobilization of antibodies. The modified steps of the WE were simulated on an ITO glass with a thickness of 0.15 mm, as shown in Figure 4B,C. Antibodies that are oriented with boric acid groups have higher activity. The ECL method was used to characterize each step of the sensing platform assembly process, as illustrated in Figure 4D. When poly-3-ABA, Ab, BSA, and progesterone were added to the sensing platform, no ECL signal was generated. However, when complex formation occurred between progesterone and the CET-Cu NCs-aptamer, the corresponding ECL signal appeared. The successful construction of the sensing platform was demonstrated.

Performance of the Sensing Platform. In the range of 0.5 pg/mL to 20 ng/mL, the logarithm of progesterone concentration was linearly correlated with the ECL signal of the sensing platform. The corresponding signal response and working curve are shown in Figure 5A,B, respectively. The

https://doi.org/10.1021/acs.analchem.3c04086
Anal. Chem. 2023, 95, 16761−16770

working curve was I_{ECL} = 1096 × lg$c$ + 1973 (R^2 = 0.994), and the detection limit was calculated to be 0.09 pg/mL. In comparison to other detection methods, our approach offers lower detection limits (Table S1). The prepared sensing platform had good specificity for progesterone. When using 100 pg/mL E2, 100 pg/mL BPA, and 100 pg/mL MC as interferents, the constructed sensing platform did not exhibit any signal response. However, when a mixture containing 100 pg/mL of E2, 100 pg/mL of BPA, 100 pg/mL of MC, and 1 pg/mL of progesterone as the analyte was tested, the sensing platform only showed a corresponding signal response to 1 pg/mL of progesterone (Figure 5C). Seven WEs were randomly selected and utilized to fabricate sensing platforms, which were employed for the consistent detection of progesterone at a concentration of 10 ng/mL. The obtained results, as illustrated in Figure 5D, exhibited remarkable consistency with an RSD below 5%. The operational stability of the sensing platform was evaluated by continuous response to 50 pg/mL of progesterone. As shown in Figure 5E, the sensing platform demonstrated excellent operational stability.

The standard addition method was used to determine the usability of the sensing platform. First, progesterone was added to the treated tap water samples, forming a series of samples with different concentrations. The treated tap water was tested by high-performance liquid chromatography, and no progesterone residue was found. A recovery test was conducted on samples with different concentrations, and it was found that the samples had a recovery rate between 93.0 and 106.6% (Table 1). It can be concluded from the experimental results that the sensing platform can be used for detecting progesterone in water.

Table 1. Recoveries of Progesterone in Samples Based on the Proposed Sensing Platform

samples	addition (ng/mL)	average (ng/mL, n = 5)	RSD (%)	recovery (%)
tap water	1.00	0.93	6.0	93.0
	5.00	4.91	2.5	98.2
	10.00	10.66	4.6	106.6

CONCLUSIONS

Highly stable CET-Cu NCs have been constructed by exploiting a supramolecular anchoring strategy. CET-Cu NCs exhibit exceptional stability together with high Φ_{ECL} and multipath ECL emission. Leveraging these remarkable properties, an ultrasensitive sensing platform for detecting progesterone has been developed by combining oriented immobilization technology and the antibody/aptamer sandwich method. To advance the application potential of Cu NCs in ECL, future efforts will involve systematic screening of superior supramolecular structures capable of effectively anchoring Cu NCs, thereby fostering innovation within the field.

ASSOCIATED CONTENT

Supporting Information

The Supporting Information is available free of charge at https://pubs.acs.org/doi/10.1021/acs.analchem.3c04086.

H-NMR of ET-Cu NCs and CET-Cu NCs; infrared spectrum of ET-Cu NCs and CET-Cu NCs; comparative experimental data of the two types of nanoclusters after 4 months of storage in aqueous phase; DPV of CET-Cu NCs; ECL−time curve of cucurbit[7]uril and ET-Cu NCs; ECL−potential curve of ET-Cu NCs; and comparison with other methods of progesterone determination (PDF)

AUTHOR INFORMATION

Corresponding Authors

Xuejing Liu − *Key Laboratory of Interfacial Reaction & Sensing Analysis in Universities of Shandong, Collaborative Innovation Center for Green Chemical Manufacturing and Accurate Detection, School of Chemistry and Chemical Engineering, University of Jinan, Jinan 250022, P. R. China;* orcid.org/0000-0003-3644-0369; Email: chm_liuxj@ujn.edu.cn

Yueyun Li − *Key Laboratory of Interfacial Reaction & Sensing Analysis in Universities of Shandong, Collaborative Innovation Center for Green Chemical Manufacturing and Accurate Detection, School of Chemistry and Chemical Engineering, University of Jinan, Jinan 250022, P. R. China; School of Chemistry and Chemical Engineering, Shandong University of Technology, Zibo 255049, P. R. China;* orcid.org/0000-0001-8558-3863; Email: liyueyun71@163.com

Qin Wei − *Key Laboratory of Interfacial Reaction & Sensing Analysis in Universities of Shandong, Collaborative Innovation Center for Green Chemical Manufacturing and Accurate Detection, School of Chemistry and Chemical Engineering, University of Jinan, Jinan 250022, P. R. China; Department of Chemistry, Sungkyunkwan University, Suwon 16419, Republic of Korea;* orcid.org/0000-0002-3034-8046; Email: sdjndxwq@163.com

Authors

Xiaoyue Zhang − *Key Laboratory of Interfacial Reaction & Sensing Analysis in Universities of Shandong, Collaborative Innovation Center for Green Chemical Manufacturing and Accurate Detection, School of Chemistry and Chemical Engineering, University of Jinan, Jinan 250022, P. R. China*

Xuan Kuang − *Key Laboratory of Interfacial Reaction & Sensing Analysis in Universities of Shandong, Collaborative Innovation Center for Green Chemical Manufacturing and Accurate Detection, School of Chemistry and Chemical Engineering, University of Jinan, Jinan 250022, P. R. China;* orcid.org/0000-0003-0310-6620

Xiang Ren − *Key Laboratory of Interfacial Reaction & Sensing Analysis in Universities of Shandong, Collaborative Innovation Center for Green Chemical Manufacturing and Accurate Detection, School of Chemistry and Chemical Engineering, University of Jinan, Jinan 250022, P. R. China;* orcid.org/0000-0002-4321-4282

Yuewei Wang − *Key Laboratory of Interfacial Reaction & Sensing Analysis in Universities of Shandong, Collaborative Innovation Center for Green Chemical Manufacturing and Accurate Detection, School of Chemistry and Chemical Engineering, University of Jinan, Jinan 250022, P. R. China*

Huangxian Ju − *Key Laboratory of Interfacial Reaction & Sensing Analysis in Universities of Shandong, Collaborative Innovation Center for Green Chemical Manufacturing and Accurate Detection, School of Chemistry and Chemical Engineering, University of Jinan, Jinan 250022, P. R. China; State Key Laboratory of Analytical Chemistry for Life Science, Department of Chemistry, Nanjing University,*

https://doi.org/10.1021/acs.analchem.3c04086
Anal. Chem. 2023, 95, 16761−16770

Nanjing 210023, China; orcid.org/0000-0002-6741-5302

Complete contact information is available at: https://pubs.acs.org/10.1021/acs.analchem.3c04086

Notes

The authors declare no competing financial interest.

■ ACKNOWLEDGMENTS

This study was supported by the National Natural Science Foundation of China (nos. 22274062, 22206056), the Natural Science Foundation of Shandong Province (no. ZR2022QB117), and the Special Foundation for Taishan Scholar Professorship of Shandong Province (no. ts20130937).

■ REFERENCES

(1) Kwak, K.; Lee, D. *Acc. Chem. Res.* **2019**, *52* (1), 12−22.
(2) Du, X.; Chai, J.; Yang, S.; Li, Y.; Higaki, T.; Li, S.; Jin, R. *Nanoscale* **2019**, *11* (41), 19158−19165.
(3) Yu, H.; Rao, B.; Jiang, W.; Yang, S.; Zhu, M. *Coord. Chem. Rev.* **2019**, *378*, 595−617.
(4) Li, D.; Chen, Z.; Mei, X. *Adv. Colloid Interface Sci.* **2017**, *250*, 25−39.
(5) Li, Q.; Mosquera, M. A.; Jones, L. O.; Parakh, A.; Chai, J.; Jin, R.; Schatz, G. C.; Gu, X. W. *ACS Nano* **2020**, *14* (9), 11888−11896.
(6) Dutta, C.; Maniappan, S.; Kumar, J. *Chem. Sci.* **2023**, *14* (21), 5593−5601.
(7) Matus, M. F.; Häkkinen, H. *Nat. Rev. Mater.* **2023**, *8* (6), 372−389.
(8) Wang, D.; Gao, X.; Jia, J.; Zhang, B.; Zou, G. *ACS Nano* **2023**, *17* (1), 355−362.
(9) Hesari, M.; Ding, Z. *J. Am. Chem. Soc.* **2021**, *143* (46), 19474−19485.
(10) Ouyang, X.; Wu, Y.; Guo, L.; Li, L.; Zhou, M.; Li, X.; Liu, T.; Ding, Y.; Bu, H.; Xie, G.; Shen, J.; Fan, C.; Wang, L. *Angew. Chem., Int. Ed.* **2023**, *62* (21), No. e202300893.
(11) Chen, S.; Huang, Z.; Jia, Q. *Sens. Actuators, B* **2020**, *319*, 128305.
(12) Wang, Y. M.; Lin, X. C.; Mo, K. M.; Xie, M.; Huang, Y. L.; Ning, G. H.; Li, D. *Angew. Chem., Int. Ed.* **2023**, *62* (9), No. e202218369.
(13) Jiao, M.; Li, Y.; Jia, Y.; Xu, L.; Xu, G.; Guo, Y.; Luo, X. *Microchim. Acta* **2020**, *187* (10), 545.
(14) Luo, W.; Wu, S.; Jiang, Y.; Xu, P.; Zou, J.; Qian, J.; Zhou, X.; Ge, Y.; Nie, H.; Yang, Z. *ACS Appl. Mater. Interfaces* **2023**, *15* (15), 18928−18939.
(15) Kim, S.; Lee, E. S.; Cha, B. S.; Park, K. S. *Nano Lett.* **2022**, *22* (15), 6121−6127.
(16) Hu, K.; Liu, Y.; Wang, Q.; Xiong, Y.; Guo, Z.; Weng, Z.; Liu, Y.; Zhang, Y.; Wu, H.; Ai, F.; Wang, X. *Chem. Eng. J.* **2023**, *463*, 142366.
(17) Lv, H.; Zhang, R.; Cong, S.; Guo, J.; Shao, M.; Liu, W.; Zhang, L.; Lu, X. *Anal. Chem.* **2022**, *94* (10), 4538−4546.
(18) Xiang, L.; Liu, L. L.; Yuan, R.; Chai, Y. Q. *Anal. Chem.* **2023**, *95* (9), 4454−4460.
(19) Zhu, X.; Liu, L.; Cao, W.; Yuan, R.; Wang, H. *Anal. Chem.* **2023**, *95* (13), 5553−5560.
(20) Wang, D.; Nie, Y.; Wang, P.; Ma, Q. *Talanta* **2023**, *258*, 124400.
(21) Wang, D.; Nie, Y.; Li, Z.; Ma, Q. *Anal. Chim. Acta* **2023**, *1238*, 340607.
(22) Shekhar, S.; Mahato, P.; Yadav, R.; Verma, S. D.; Mukherjee, S. *ACS Sustainable Chem. Eng.* **2022**, *10* (4), 1379−1389.
(23) Mukhopadhyay, R. D.; Kim, K. *Nat. Chem.* **2023**, *15* (3), 438.
(24) Wang, Z.; Sun, C.; Yang, K.; Chen, X.; Wang, R. *Angew. Chem., Int. Ed.* **2022**, *61* (38), No. e202206763.
(25) Zhang, X.; Jia, Y.; Feng, R.; Wu, T.; Zhang, N.; Du, Y.; Ju, H. *Anal. Chem.* **2023**, *95* (2), 1461−1469.
(26) Ojoghoro, J. O.; Scrimshaw, M. D.; Sumpter, J. P. *Sci. Total Environ.* **2021**, *792*, 148306.
(27) Azizi-Lalabadi, M.; Pirsaheb, M. *Process Saf. Environ.* **2021**, *152*, 14−24.
(28) Qasim, S.; Hsu, S. Y.; Rossi, E.; Salahshoor, Z.; Lin, C. H.; Parada, L. P.; Fidalgo, M. *Microchim. Acta* **2022**, *189* (5), 174.
(29) Ge, C.; Feng, J.; Zhang, J.; Hu, K.; Wang, D.; Zha, L.; Hu, X.; Li, R. *Talanta* **2022**, *236*, 122847.
(30) Aubret, M.; Savonnet, M.; Laurent, P.; Roupioz, Y.; Cubizolles, M.; Buhot, A. *Anal. Chem.* **2022**, *94* (7), 3376−3385.
(31) Zhu, Y.; Xu, Z.; Gao, J.; Ji, W.; Zhang, J. *Biosens. Bioelectron.* **2020**, *160*, 112210.
(32) Wang, Y.; Zhao, G.; Chi, H.; Yang, S.; Niu, Q.; Wu, D.; Cao, W.; Li, T.; Ma, H.; Wei, Q. *J. Am. Chem. Soc.* **2021**, *143* (1), 504−512.
(33) Tan, X.; Zhang, B.; Zou, G. *J. Am. Chem. Soc.* **2017**, *139* (25), 8772−8776.
(34) Ru, Z.; Jia, Y.; Du, Y.; Han, Y.; Zhang, N.; Ren, X.; Wei, Q. *Anal. Chem.* **2023**, *95* (27), 10178−10185.
(35) Rizzo, F.; Polo, F.; Bottaro, G.; Fantacci, S.; Antonello, S.; Armelao, L.; Quici, S.; Maran, F. *J. Am. Chem. Soc.* **2017**, *139* (5), 2060−2069.
(36) Alt, K.; Carraro, F.; Jap, E.; Linares-Moreau, M.; Riccò, R.; Righetto, M.; Bogar, M.; Amenitsch, H.; Hashad, R. A.; Doonan, C.; Hagemeyer, C. E.; Falcaro, P. *Adv. Mater.* **2022**, *34* (21), 2106607.